

Effect of the Sampling Parameters in FOCV-MPPT Circuits for Fast-Varying EH Sources

Matias Carandell, Andrew S. Holmes, *Member, IEEE*, Daniel Mihai Toma, Joaquín del Río, *Senior Member, IEEE*, and Manel Gasulla, *Senior Member, IEEE*,

Abstract— The fractional open circuit voltage (FOCV) method is extensively used in low-power energy harvesting (EH) sources to extract maximum power. For fast-varying EH sources a fast sampling rate is required. This work theoretically analyzes the influence of the sampling time and period on the harvested power of sinusoidal EH sources. In addition, the circuit limitations to achieve a fast sampling rate are presented and circuits to deal with them proposed and implemented. Furthermore, one of the circuits is based on a novel pseudo-FOCV method and achieves the fastest sampling rate. Experimental tests are performed with a 2 Hz, 1 V to 3 V sinusoidal source having an output resistance of 127 Ω , and the results are shown to agree with theoretical predictions. It is shown that 1) the harvested power increases with the sampling rate when the sampling time is negligible (sampling 15 times faster than the source frequency extracts around 99 % of the maximum), and 2) for fixed sampling times there is an optimum sampling rate where the harvested power is maximum. The first result is generic and valid for methods other than the FOCV. Tests were also performed with a small-scale wave energy converter placed in a linear shaker emulating a sea environment. Harvested power increases by 25 % with respect using a commercial FOCV unit with a low sampling rate.

Index Terms— Energy Harvesting, Fractional Open Circuit Voltage, Maximum Power Point Tracking, Power Management Unit, Wave Energy Converter and Wireless Sensor Networks.

I. INTRODUCTION

WIRELESS sensor networks (WSN) are becoming ever more prevalent with the implementation of IoT solutions. Supplying power to the sensor nodes is one of the key challenges in WSN design. Batteries have a limited energy and have to be periodically replaced, which can be costly and even unfeasible. In contrast, energy harvesting (EH) can provide unlimited energy. However, EH sources require an additional power management unit (PMU) to convert their variable output to a constant and clean supply to feed the sensor nodes. PMUs should also manage any power mismatch between the source and the load by including an energy storage element (ESE) where energy can be stored or dispatched as required. An additional function of the PMU is maximum power point tracking (MPPT) to continuously ensure the maximum available energy is harvested from the EH source.

One simple MPPT approach, widely used in low-power EH applications and also implemented in commercial chips, such as in [1], is the fractional open circuit voltage (FOCV) method.

This method, thoroughly explained in [2], exploits the nearly linear relationship between the maximum power point (MPP) voltage (V_{MPP}) and the open circuit voltage (V_{OC}) of the EH source. Maximum energy is harvested by fixing the output voltage of the EH source to V_{MPP} , which is a percentage of its V_{OC} ; this percentage is typically 50% for thermoelectric, piezoelectric or radio frequency sources, and 60-80% for photovoltaic (PV) sources. Typically, V_{OC} is periodically measured (at a sampling period of T_{MPPT}) by momentarily disconnecting the EH source from the PMU during a sampling time (t_{SAMP}) and storing the V_{OC} corresponding to the new environmental conditions.

Some sources, such as wind energy harvesters (WEH) or wave energy converters (WEC), require fast tracking of the MPP because V_{OC} shows relatively rapid variations. For example, [3] and [4] present a WEH and a WEC respectively, each with V_{OC} oscillating at around 1.8 Hz; this is fast-varying compared to other types of EH sources such as thermoelectric or PV devices. In [5], it was experimentally demonstrated that, by increasing the sampling rate ($f_{MPPT} = 1/T_{MPPT}$) of a PMU working with a WEC oscillating at 2 Hz, the total harvested energy improved up to 25%. A similar conclusion was reached in [6], where increases of 22 % and 44 % in the extracted energy were achieved for weakly- and strongly-coupled piezoelectric vibration harvesters respectively. In both cases, the increase of energy captured would help expand the autonomy of EH-powered WSN nodes. However, increasing f_{MPPT} can also reduce the harvested energy due to the losses associated with momentarily disconnecting the EH source each sampling event.

There are two approaches for implementing a FOCV-MPPT circuit: resistor-based [7]–[11] and capacitor-based [12]–[14]. The former uses a resistor divider to generate the desired fraction of V_{OC} while in the latter this is achieved by charge-sharing. In general, resistor-based circuits offer greater precision in the MPP tracking and require a smaller number of switches. On the other hand, capacitor-based circuits allow a fast charging of the sampling capacitor, leading to a drastic reduction of t_{SAMP} .

Implementations of fast-sampling resistor-based FOCV-MPPT methods ($f_{MPPT} \geq 1$ Hz) dedicated to low-power EH sources (output power below 10 mW) can be found in the literature. Refs. [7] and [8] deal with PV sources achieving

This work was supported by the project MELOA from the European Commission's Horizon 2020 research and Innovation program under Grant Agreement No. 776280 and by the Spanish Ministry of Economy and Competitiveness and the European Regional Development Fund under project TEC2016-76991-P. The first author has a grant from the Secretariat of

Universities and Research of the Ministry of Business and Knowledge of the Government of Catalonia on the FI program (ref. BDNS 362582).

M.C., D.T., J.R., and M.G. authors are with the Department of Electronics Engineering from Universitat Politècnica de Catalunya (UPC) at Spain (e-mail: matias.carandell@upc.edu). A.H. author is with the Department of Electrical and Electronic Engineering, Imperial College London, UK.

TABLE I. FAST-SAMPLING, RESISTOR-BASED FOCV-MPPT WORKS FOR LOW-POWER ENERGY HARVESTING SYSTEMS

Ref.	EH source and frequency	Input voltage	$t_{\text{SAMP}} / T_{\text{MPPT}}$
[7]	Solar PV	2-5 V	5 ms / 100 ms
[8]	Solar PV	2-4 V	33 μs / 3.33 ms
[9]	PZT @ 80 Hz	1-3 V	15 ms / 1 s
[10]	Solar PV	> 10 mV	10 ms / 150 ms
[11]	Solar PV	0.1 – 3 V	Variable ~ - / 25 ms
This work (Config. C)	WEC @ 1.8 Hz	0.08 – 3.3* V	0.32 μs / -

PZT: Piezoelectric device, *Set by the PMU IC (ADP5092)

sampling times/periods ($t_{\text{SAMP}}/T_{\text{MPPT}}$) of 5 ms/100 ms and 33 μs /3.33 ms, respectively. In [9], a vibrational EH source using a piezoelectric (PZT) device is used, where the PMU refreshes the MPP after the PZT voltage rectification step with $t_{\text{SAMP}}/T_{\text{MPPT}}$ of 15 ms/1 s. A boost converter was used in [10] to harvest energy from PV cells with very low input voltages and with $t_{\text{SAMP}}/T_{\text{MPPT}}$ of 10/150 ms. In [11], also dealing with PV applications, changes in the solar irradiance are detected on the input voltage using a custom circuit that makes T_{MPPT} variable around 25 ms. TABLE I, summarizes these works, showing in each case the EH source and frequency, input voltage range and sampling time and period.

Although these works have successfully implemented fast MPPT circuits for low-power applications, the effect of the sampling parameters (t_{SAMP} and T_{MPPT}) on the power extraction has not been studied in depth. Just in [15], Balato et al. optimized the parameters of the FOCV method to maximize the power extracted from resonant piezoelectric vibration harvesters after an AC/DC bridge rectification step. However, the parameter t_{SAMP} was kept constant to 0.3 s in the analysis and only variations in T_{MPPT} were considered. Furthermore, the acceleration amplitude was modulated by a slow 50 s period saw-tooth waveform, so a fast sampling rate was not required since the optimum T_{MPPT} value was 16.7 s.

Several companies offer PMU ICs with resistor-based FOCV-MPPT for very low-power EH applications. The BQ25504/5 (*Texas Instruments*) and the ADP5091/2 (*Analog Devices*) are two of the most widely-used devices. They both offer efficient power extraction (>80 %) from microwatts to milliwatts at a very low input voltage (<100 mV) with ultra-low quiescent currents (<500 nA). However, the T_{MPPT} is fixed to 16 s, which is too slow for fast-varying EH sources. The recently launched AEM30330 (*e-Peas*) is another PMU IC with T_{MPPT} down to 18 ms. However, t_{SAMP} is 3.8 ms representing up to

20% of the operation time, which drastically reduces its overall efficiency.

This paper analyzes the influence of the sampling parameters on the harvested power from a sinusoidal EH source, presents the circuit limitations for achieving fast-sampling, and proposes and tests three circuits to deal with them. Furthermore, one of them is based on a new pseudo-FOCV method. The focus is on resistor-based FOCV, but some analytical results presented are also valid for capacitor-based circuits and even for any MPPT method. Experimental tests are performed which agree well with the theoretical predictions. One of the tests includes a WEC with accelerations of 2 Hz.

II. FAST-TRACKING FOCV METHODS: PRINCIPLE, HARVESTED POWER, ARCHITECTURE, AND LIMITATIONS

A. Principle

For applications with a fast-varying EH source it is necessary to increase the sampling rate of V_{OC} to maintain a good MPPT performance. This can be understood with the aid of Fig. 1 (left) which shows a sinusoidal V_{OC} with offset waveform (top curve), found in some WEC harvesters [4], with the following expression:

$$V_{\text{OC}}(t) = V_{\text{DC}} + V_{\text{AC}} \sin\left(\frac{2\pi t}{T_{\text{EH}}}\right) \quad (1)$$

where V_{DC} and V_{AC} are the DC offset and sinusoidal amplitude of V_{OC} , respectively, and T_{EH} is the source period. Also shown in Fig. 1 is the loaded EH output voltage under ideal MPPT conditions; V_{MPP} (50 % of V_{OC} in this example, in the bottom part), and the actual EH output voltage (V_{GEN}) for two different sampling periods and assuming the FOCV-MPPT method. Sampling rates of 12 and 3 samples per period of the sinusoid are represented with solid ($V_{\text{GEN}1}$) and dashed ($V_{\text{GEN}2}$) staggered lines respectively. V_{GEN} is set equal to 50% of V_{OC} at each sampling point, and then held constant until the next sampling event during a time t_{HARV} . As can be seen, the faster the sampling rate, the more time V_{GEN} spends near V_{MPP} and, therefore, the more energy will be extracted. However, as can be seen in more detail in Fig. 1 (right, inset zoom of the left side), some time is spent in the sampling event (t_{SAMP}), during which the EH source is open-circuit, and no energy is harvested. During t_{SAMP} , V_{GEN} reaches V_{OC} , follows it, and finally drops to the new V_{MPP} (here $V_{\text{MPP}1}$ and $V_{\text{MPP}2}$). Note that these positive excursions in V_{GEN} during sampling are omitted from the left-hand figure for clarity.

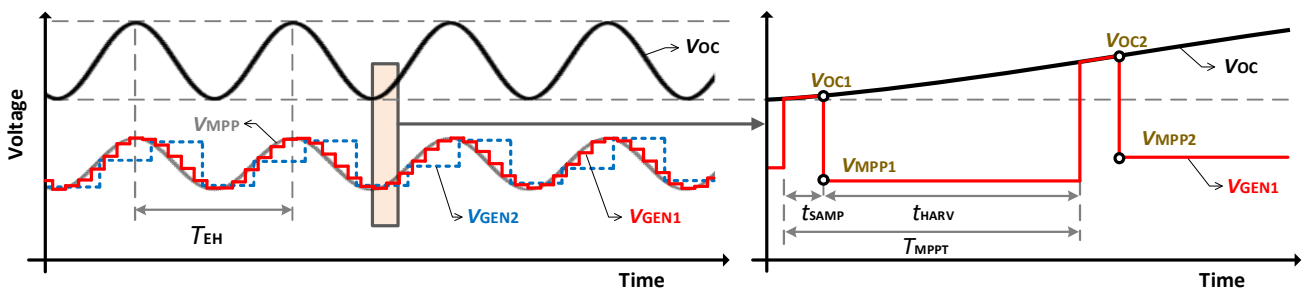


Fig. 1. Left: Sinusoidal V_{OC} waveform with positive offset for a harvester (top line), the corresponding ideal V_{MPP} ($1/2 V_{\text{OC}}$) and the EH output (V_{GEN}) for two sampling periods (solid and dashed staggered lines) using the FOCV-MPPT method. Right: an inset zoom showing V_{OC} and V_{GEN} for the fastest sampling rate.

B. Harvested power

Harvested power can be maximized by working at the MPP but it also depends on t_{SAMP} and T_{MPPT} , as will be shown. For the sake of simplicity, a Thévenin equivalent for the EH source is assumed consisting of a voltage source V_{OC} in series with an internal resistor R_{G} . This is the case for several types of EH sources (e.g., thermoelectric, electromagnetic, radiofrequency), including that used later in Section V.C. For these sources, maximum power is achieved when $V_{\text{MPP}} = 0.5 \cdot V_{\text{OC}}$, as stated by the maximum power transfer theorem [16]. Assuming (1) for V_{OC} , the maximum average power is given by

$$P_{\text{MPP}} = \frac{\overline{V_{\text{OC}}^2}}{4R_{\text{G}}} = P_{\text{DC}} \left[1 + \frac{\alpha^2}{2} \right] \quad (2)$$

where $P_{\text{DC}} = \frac{V_{\text{DC}}^2}{4R_{\text{G}}}$, $\alpha = \frac{V_{\text{AC}}}{V_{\text{DC}}}$, and the overbar denotes a time average over one source period. However, this result is achieved when no sampling effect is considered. The Appendix presents an analytical derivation for obtaining the approximate power given to a load (P_{LOAD}) considering the sampling process, leading to:

$$P_{\text{LOAD}} \approx P_{\text{DC}} \left\{ \left[(7 + 3r_{\text{S}}) \frac{128}{45} \alpha^2 \right] r_{\text{M}}^4 - \left[\frac{64}{9} \alpha^2 \right] r_{\text{M}}^2 + \left[1 + \frac{8}{15} \alpha^2 \right] (1 - r_{\text{S}}) \right\} \quad (3)$$

where $r_{\text{S}} = \frac{t_{\text{SAMP}}}{T_{\text{MPPT}}}$ and $r_{\text{M}} = \frac{T_{\text{MPPT}}}{T_{\text{EH}}}$. The parameter r_{S} denotes the time percentage the circuit is sampling and thus not harvesting, whereas the inverse of r_{M} denotes the number of samples per period of the signal source. The approximate form in (3) is applicable when $r_{\text{S}} \ll r_{\text{M}} \leq 0.25$. For $r_{\text{S}}, r_{\text{M}} \rightarrow 0$ (negligible sampling time and infinite sample rate), we get

$$P_{\text{LOAD}} = P_{\text{MAX}} = P_{\text{DC}} \left[1 + \frac{8\alpha^2}{15} \right] \quad (4)$$

which slightly differs from (2) because in the Appendix a piecewise quadratic approx. is used for V_{OC} instead of (1).

Fig. 2 shows P_{LOAD} normalized to P_{MAX} versus $1/r_{\text{M}}$ for several sampling scenarios, according to (3) and using $\alpha = 0.5$. When r_{S} is constant (square markers), the normalized power rises to a maximum as $1/r_{\text{M}}$ increases. In addition, the lower r_{S} , the lower the losses due to disconnection of the EH source during sampling, and the higher the power. In fact, for $1/r_{\text{M}} \rightarrow \infty$, from (3), the relative power loss is r_{S} . For $r_{\text{S}} \rightarrow 0$, around 99% of the maximum power is harvested when sampling 15 times

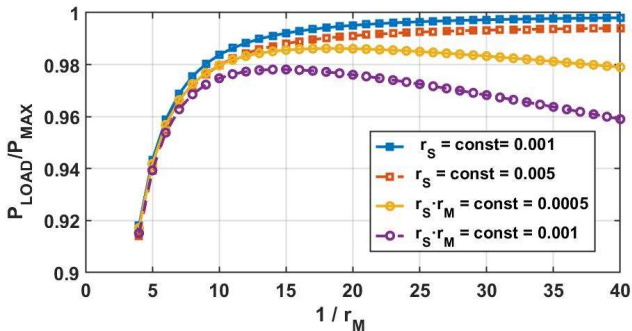


Fig. 2. P_{LOAD} normalized to P_{MAX} versus $1/r_{\text{M}}$ for different sampling scenarios, according to (3) using $\alpha=0.5$.

faster than the source frequency ($f_{\text{MPPT}} = 15 \cdot f_{\text{EH}}$). This result is also valid for MPPT methods other than the FOCV. On the other hand, when $r_{\text{S}} r_{\text{M}} = \frac{t_{\text{SAMP}}}{T_{\text{EH}}}$ is constant (circle markers), i.e.

t_{SAMP} and T_{EH} are fixed, increasing $1/r_{\text{M}}$ increases further r_{S} and thus the percentage of time sampling without harvesting energy from the EH source. In this case, there is an optimum value of r_{M} where the normalized power is maximum; this maximum power is higher and the optimum r_{M} lower for lower values of $r_{\text{S}} r_{\text{M}}$. A similar behavior was observed in [15].

C. Architecture

In resistor-based FOCV circuits, a resistor divider is used to generate the desired fraction of V_{OC} and then store it in a sampling capacitor (C_{SAMP}).

Fig. 3 shows the block diagram of a standard PMU with this FOCV configuration. An EH source is connected at the input (here a Thévenin equivalent) whereas an ESE and a load are connected at the output. This work focuses on the sample and hold (S&H) circuit of the MPPT controller, which is highlighted inside the PMU box. However, it is noted that the PMU includes other functionalities, the most important being DC/DC conversion and control of power flow between the EH source, the ESE and the LOAD (e.g. a sensor node) depending on the available harvested power, the load requirements, and the state of charge of the ESE.

At the PMU input (V_{GEN}), a capacitor C_1 is placed as a buffer between the PMU and the EH source. Further, two more capacitors (C_2 and C_3) are placed at the ESE (V_{BAT}) and LOAD (V_{LOAD}), respectively. At each sampling event, the PMU IC opens the switch S_1 and closes switch S_3 during t_{SAMP} . Thus, V_{GEN} rises to V_{OC} (right side of Fig. 1), the sampled V_{MPP} appears at the output of the resistive divider formed by R_1 and R_2 and is stored at C_{SAMP} . Then, during t_{HARV} , S_1 closes and S_3 opens, and the PMU forces V_{IN} to the last sampled value of V_{MPP} by periodically moving energy from C_1 to C_2 and C_3 .

D. Limitations

Fig. 2 shows that to increase harvested power both r_{S} and r_{M} must be small, with $t_{\text{SAMP}} \ll T_{\text{MPPT}} \ll T_{\text{EH}}$. During t_{SAMP} , C_{SAMP} must be updated to a new value of V_{MPP} . In order for the error in the sampled voltage to be e.g. $< 1\%$, we require the charging ratio $r_{\text{C}} = \frac{t_{\text{SAMP}}}{\tau}$ to be higher than 4.6. The time constant τ is defined as $\tau = R_{\text{TH}} C_{\text{SAMP}}$ where R_{TH} is equivalent to R_1 in parallel with R_2 , assuming the equivalent output resistance of the EH source (R_{G}) negligible. Thus, for a fixed value of r_{C} , a reduction of t_{SAMP} implies decreasing τ and therefore either R_{TH} or C_{SAMP} .

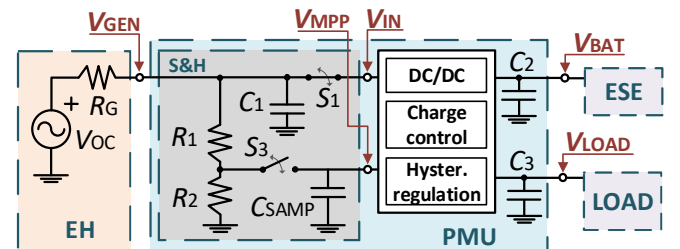


Fig. 3. Standard PMU architecture implementing a resistor-based S&H circuit for a FOCV-MPPT. An EH source (input), and an ESE and a LOAD (output) are also represented.

On the one hand, R_{TH} can be reduced by reducing the values on the resistor divider. This leads to a reduction of the global efficiency because the resistor divider is always connected to V_{GEN} and consuming power. Thus, $R_1+R_2 \gg R_G$ is required. In this way, an accurate V_{MPP} is also attained. On the other hand, reducing C_{SAMP} has two potential limitations. First, it must hold V_{MPP} during t_{HARV} in spite of any leakage current at the PMU pin connected to C_{SAMP} . Second, C_{SAMP} must deal with the charge injection produced by S_3 . It is worth noting that the constraints on the R and C values resulting from the need for low power consumption and capacitive storage of the sampled voltage are particular to the PMU application; they do not apply to other sampling systems such as commercial voltage probes, and consequently these can readily achieve much shorter sampling times.

Several ideas can be found in the literature to deal with these issues. In [10], a third switch is added to the standard resistor-based S&H circuit (Fig. 3). This switch disconnects the S&H circuit during t_{HARV} , leading to a reduction of power losses. Then, the resistor divider values can also be decreased to reduce τ , allowing faster sampling rates. A solution to solve the problem of leakage on C_{SAMP} has been presented in [11] and [14]. Both works share the same idea even though [11] is resistor-based and [14] is capacitor-based. It consists of comparing the sampled V_{MPP} with a number of fixed voltage references from a resistor string and choosing the one closest to the new V_{MPP} . This is a complex solution that also adds the error of the resistor string accuracy. Finally, a solution for the problem of the charge injection on C_{SAMP} has been proposed in [12], where a pair of dummy switches driven in counter-phase mitigate the increase of voltage on the sampling capacitor.

Commercial solutions such as the ADP5092 offer relatively large sampling times and periods of $t_{SAMP} = 256$ ms and $T_{MPPT} = 16$ s ($r_S = 1.6$ %), which are inadequate for applications requiring fast-sampling. These large times derive from the suggested values for R_1+R_2 (20 M Ω) and C_{SAMP} (10 nF), leading to $\tau = 50$ ms (with $R_1 = R_2$, worst case) and $r_C = 5.12$.

III. PROPOSED CONFIGURATIONS

This section presents three proposed fast-sampling PMU configurations (section III.A) followed by their S&H circuit design (section III.B) and practical implementation (section III.C).

A. Reference and proposed fast-sampling configurations

In this work, a typical configuration of the ADP5092, such as the one found in its evaluation board (EB-ADP5092), was used as the *reference* configuration (config. R hereafter) to be compared with three new proposed and fast-sampling PMU configurations where t_{SAMP} and T_{MPPT} are greatly reduced to achieve low values of r_S and r_M . These units include the ADP5092 IC, to take advantage of its robustness and ultra-low power consumption, and additional low-power sampling circuitry, to drastically increase the sampling rate with respect to config. R.

Fig. 4 shows schematics of the 4 PMU configurations. Just the S&H circuit changes between configurations (central box). At the input, the WEC model reported in [17] is placed, which consists of a Thévenin equivalent generating a sinusoidal voltage as in (1). An R_G of 127 Ω , similar to the value reported in [17], is used in the following sections. For the ESE, a 165 mAh – 3.7 V Li-Ion polymer battery charged to 3.8 V is selected and no load is connected to the SYS pin. So, the output power is only delivered to the ESE. The resistor divider is set to 50 % ($R_1 = R_2$). Nine test points are used for the analysis of the PMU performance. Four are common: V_{GEN} , V_{BAT} , I_{IN} (input current), and I_{OUT} (output current); four are specific of the proposed configurations (A, B, and C): V_{DIV} (junction of R_1 and R_2), V_{MPP} , V_{IN} , and V_{PULSE} (sampling control signal); one more is only used for config. B: V_{OA} . Config. R works as previously described in Section III.C. In the proposed configurations, the MPPT pin was left floating since V_{MPP} is provided to C_{SAMP} at the CBP pin through the external switch S_3 , which works as described in Section II.C. Next, the particularities of the proposed configurations are described.

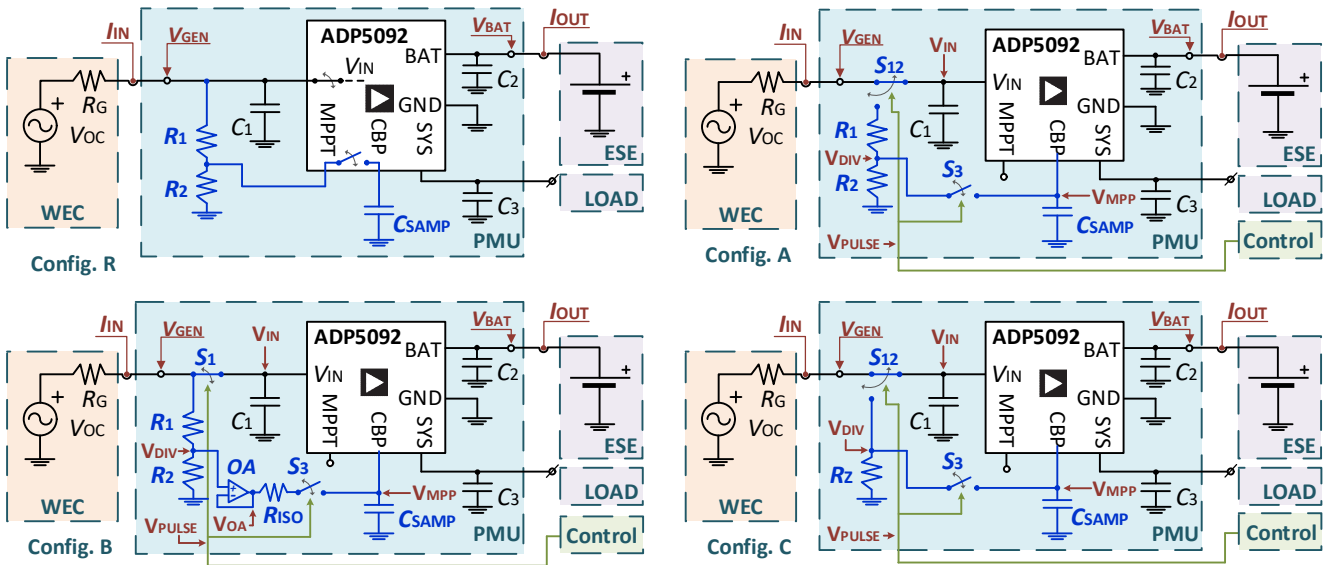


Fig. 4. Proposed PMU configurations: Reference (top left), A (top right), B (bottom left), and C (bottom right). All configurations include the WEC electrical model as the input source and an ESE as the sole output load.

1) *Config. A.* A single pole double throw (SPDT) switch S_{12} connects V_{GEN} with either V_{IN} or the resistor divider. During t_{SAMP} , V_{GEN} connects to the resistor divider, leaving V_{IN} floating. Then, during t_{HARV} , S_{12} re-connects V_{GEN} with V_{IN} , disconnecting the resistor divider to avoid losses. So, R_1 and R_2 can be small to reduce t_{SAMP} and achieve a fast MPPT while resistive power losses are kept small. This configuration is similar to that implemented in [10] with a different distribution of the switches.

2) *Config. B.* An operational amplifier (OA) working as a voltage follower is included with a series resistor (R_{ISO}) to faster stabilize its output (V_{OA}). C_{SAMP} is directly charged from the OA output, so that its charging time and thus t_{SAMP} mainly depends on the slew rate (SR) and OA bandwidth. Thus, R_1 and R_2 can be increased again to minimize losses without affecting t_{SAMP} , as long as the effect of the OA input parasitic capacitance (C_{OA}) is neglectable.

3) *Config. C.* During t_{SAMP} , S_{12} connects V_{GEN} to an impedance reference R_Z ($=R_G$), so that V_{DIV} and V_{MPP} remain as $V_{OC}/2$. Thus, the WEC must be previously characterized to know R_G and this value should not change significantly over time. During t_{HARV} , S_{12} connects V_{GEN} to V_{IN} , disconnecting R_Z . Given R_Z is small, t_{SAMP} can be drastically reduced. This configuration constitutes a novel MPPT method not reported in earlier works and inspired by the working mode of the *e-Peas* chips. It combines the MPPT techniques of resistor emulation [18] and FOCV.

B. S&H circuit values

In order to keep the power losses small, appropriate values of R_1 , R_2 and C_{SAMP} must be used in all configurations. Config. C does not use R_1 and R_2 but $R_Z = R_G$. It will be assumed that each loss factor leads to a maximum power loss of εP_{MPP} with $\varepsilon \ll 1$. First, power is wasted in R_1 and R_2 , but they are permanently connected (and in particular during t_{HARV}) just in configs. R and B. Thus, we require $R_1 + R_2 \geq R_G/\varepsilon$ for these two configurations. Second, errors in the determination of V_{MPP} also lead to a power reduction that applies to all configurations. Assuming the Thévenin equivalent for the energy source, his instantaneous delivered power must satisfy:

$$\frac{[V_{OC} - V_{GEN}]V_{GEN}}{R_G} \geq (1 - \varepsilon) \frac{V_{OC}^2}{4R_G} \quad (5)$$

which is a quadratic inequality that can be easily solved in

$$\frac{V_{OC}}{2}(1 - \sqrt{\varepsilon}) \leq V_{GEN} \leq \frac{V_{OC}}{2}(1 + \sqrt{\varepsilon}) \quad (6)$$

Errors in V_{MPP} can have three causes: 1) loading effect of R_G when using R_1 and R_2 (in all configurations except config. C), 2) leakage current (I_{leak}) from the ADP5092 CBP pin on C_{SAMP} , and 3) charge injection effect (ΔQ) on C_{SAMP} due to the internal switch in config. R and S_3 in the proposed configurations. After some processing, it is found that the following conditions must be met to accomplish (6): $R_1 + R_2 \geq R_G(1 - \sqrt{\varepsilon})/\sqrt{\varepsilon}$ by cause 1, $C_{SAMP} \geq I_{leak} \cdot T_{MPPT}/(\varepsilon \cdot V_{MPP})$ by cause 2, and $C_{SAMP} \geq \Delta Q/(\varepsilon \cdot V_{MPP})$ by cause 3.

As an example, $\varepsilon = 0.1\%$ is assumed. Thus, $R_1 + R_2 \geq 1000R_G$ for configs. R and B. On the other hand, according to cause 1, $R_1 + R_2 \geq 30.65 \cdot R_G$ for all configs. except C, which is less

restrictive than the previous condition, so it only applies to config. A. Assuming $R_1 = R_2$, the minimum value of τ (τ_{min}) is $250 \cdot R_G \cdot C_{SAMP}$ for configs. R and B, $7.66 \cdot R_G \cdot C_{SAMP}$ for config. A, and just $0.5 \cdot R_G \cdot C_{SAMP}$ for conf. C. So, config. C has more room for the reduction of τ and thus for faster sampling rates.

As for C_{SAMP} , assuming $V_{MPP} = 1V$ (typical in small-scale WECs according to [4]) and $I_{leak} = 10$ pA (typical value of the ADP5092), $C_{SAMP} = 316.5 \cdot T_{MPPT}$ (in pF). For config. R ($T_{MPPT} = 16$ s) this leads to $C_{SAMP} \geq 5$ nF (10 nF recommended by the ADP5092). Instead, in the proposed configurations and assuming $r_M = 0.1$ with $f_{EH} = 1/T_{EH} = 1.8$ Hz [3], [4], $C_{SAMP} \geq 17.5$ pF, so much lower. On the other hand, considering $\Delta Q = 5$ pC (feasible value for commercial switches), $C_{SAMP} \geq 158$ pF in all configurations. Lower values of V_{MPP} would lead to higher values of C_{SAMP} in all cases.

C. Implementation of the PMUs

A generic modular circuit board was produced to hold the three proposed PMU configurations, which includes the ADP5092 IC and the additional sampling circuitry (Fig. 4). The voltage test points were included in the board and the current test points (I_{IN} and I_{OUT}) were external. The active components included in the new configurations (OA, S_3 and S_{12} or S_1) were internally fed from the ESE.

TABLE II lists the components of the sampling circuitry used for each of the four PMU configurations. As can be seen, in configs. R and B the standard values proposed by the ADP5092 manufacturer were used for R_1 and R_2 (10 M Ω) and C_{SAMP} (10 nF) whereas lower values were used for config. A (100 k Ω , 1.2 nF). Other required components were chosen following the manufacturers' recommendations, as for example $C_1 = 10 \parallel 0,1$ μ F, $C_2 = 220$ uF, and $C_3 = 4.7$ uF. The active components of the proposed configurations were carefully chosen to be low-power devices. For the OA, a MAX40007 (*Maxim*, 0.7 μ A of typical supply current, rail-to-rail output) was selected. A low switching time and on-state resistance (R_{ON}) are sought for the switches. In particular, $R_{ON} \ll R_G$ for S_{12} and S_1 to reduce losses during t_{HARV} and for S_{12} in config. C to set an accurate V_{MPP} during t_{SAMP} . For S_3 , R_{ON} adds during t_{SAMP} to $R_1 \parallel R_2$ in config. A, and to $R_G \parallel R_Z$ in config. C, thus also contributing to τ . A low charge injection is sought for S_3 to minimize its effects at C_{SAMP} after the sampling time. For S_{12} , a MAX4714 (*Maxim*, 0.04 μ A, 13 ns, 0.6 Ω) was selected, for S_1 a MAX4716 (*Maxim*, 0.04 μ A, 12 ns, 0.3 Ω), and for S_3 a MAX4594 (~0.02 μ A, 25 ns, 6.5 Ω , 2pC).

TABLE II. COMPONENT LIST FOR EACH PMU CONFIGURATION

	Config. R	Config. A	Config. B	Config. C
S_{12} / S_1	-	MAX4714	MAX4716	MAX4714
S_3	-	MAX4594	MAX4594	MAX4594
R_1 / R_2	10 M Ω	100 k Ω	10 M Ω	-
OA	-	-	MAX40007	-
R_{ISO}	-	-	3,3 k Ω	-
R_Z	-	-	-	127 Ω
C_{SAMP}	10 nF	1.2 nF	10 nF	10 nF
τ	50 ms	60 μ s	7.5*/10.6** μ s	0.7 μ s

*Calculated with the OA input capacitance instead C_{SAMP} .

**Derived from the OA bandwidth

TABLE II also shows the resulting values of τ . As can be seen, config. R presents a value much higher than the proposed configurations. In config. B, the OA buffers C_{SAMP} and τ is thus calculated as $R_{TH}C_{OA}$ ($C_{OA} = 1.5$ pF), which allows high values for R_1 and R_2 while still achieving a low value of τ , in particular $\tau = 7.5$ μ s. But the OA bandwidth (15 kHz) leads to a time constant $\tau_{OA} = 10.6$ μ s, so more restrictive. In addition, the SR (12 V/ms) needs also to be considered for large signal variations. Config. C uses $R_Z = R_G$ (127 Ω , 0.1%) and thus $\tau = 0.7$ μ s (accounting also for the series R_{ON} of S_3).

For the case of $R_G = 127$ Ω , following the design rules of section III.B for R_1 and R_2 and setting $C_{SAMP} = 1$ nF (accounting for a value of V_{MPP} even lower than 1 V) the resulting values of τ_{min} are 32 μ s, 972 ns, and 70 ns for configs. R, A, and C (with the effect of S_3 included), respectively. A τ of 48 ns results for config. B with $C_{OA} = 1.5$ pF but parasitic capacitances can significantly increase this value. Furthermore, the limiting factor will be the OA bandwidth ($\tau_{OA} = 10.6$ μ s) and SR. With $r_C = 4.6$, t_{SAMP} results in 147 μ s, 4.47 μ s, 48.8 μ s, and 322 ns for config. R, A, B, and C, respectively. Thus, all the proposed configurations achieve a lower t_{SAMP} than config. R, and in particular config. C achieves a near 500-fold decrease, thus allowing very fast-sampling. This configuration is also added at the end of TABLE I to compare it with the literature works presented in Section I. As can be seen, the achieved value of t_{SAMP} is greatly reduced compared with the previous reported fast-tracking works, and in particular is 100 times smaller than that of [8], which presented the smallest value of t_{SAMP} . No value is shown for T_{MPPT} since it depends on the value of r_S .

IV. PERFORMANCE OF THE SAMPLING CIRCUITRY

The performance of the additional sampling circuitry of the proposed configurations was tested using the components of TABLE II. An HP33120A function generator (FG) with an internal output resistance of 50 Ω was used with an external 77- Ω series resistor giving a total resistance of ~ 127 Ω , in order to

emulate the WEC. The FG was set with a voltage step from 0 V to 3 V (V_{OC}), which was selected considering [4]. V_{PULSE} was provided by a DAQ (USB-6216, National Instruments) and was configured to provide $T_{MPPT} = 24$ ms and $t_{SAMP} = 0.5$ ms, which leads to $r_S = 2.1$ %, similar to that of the config. R (1.6 %). With these values, r_C results in 8.3, 67 and 700 for config. A, B, and C, respectively, ensuring an accurate V_{MPP} ($r_C > 4.6$) in all cases. Then, the dynamic behavior of the voltage test points (except V_{BAT}) was observed and the main sampling parameters identified.

A four-channel oscilloscope (Lecroy Wavesurfer 3024) was used to measure the voltage test points; the high-impedance points (V_{DIV} and V_{MPP}) were buffered with an external OA (TL064CN). Fig. 5 shows the temporal profile of the signals. The plots on left and right show respectively zoomed-out & zoomed-in views during the sampling process. Each pair of plots corresponds to a different PMU configuration.

The left plots show all the signals except V_{MPP} . A V_{PULSE} of 0.5 ms (t_{SAMP}) is observed (T_{MPPT} of 24 ms not shown). During t_{SAMP} and for config. A and B, V_{GEN} is disconnected from V_{IN} and rises from the previous MPP value (0 V in this test) to the current V_{OC} (3 V) whereas V_{IN} remains at 0 V. Meanwhile, V_{DIV} rises from 0 V to 1.5 V with a theoretical $\tau = 60$ μ s for config. A. For config. B, τ is higher than predicted because of the parasitic capacitance of the external buffer OA. V_{OA} follows V_{DIV} with a slope limited by the OA SR. For config. C, V_{GEN} is directly connected to V_{DIV} and both rise abruptly to 1.5 V since now $\tau = 0.7$ μ s, much smaller.

For all configurations, V_{GEN} is re-connected to V_{IN} after t_{SAMP} and falls to 0 V (present value at C_1) before rising with a nominal time constant of 1.27 ms ($C_1 = 10$ μ F and $R_G = 127$ Ω) to settle at the new V_{MPP} (1.5 V). After this, a small ripple appears (only shown in an inset zoom of config. B plot) between two threshold values around V_{MPP} , typical of the energy transfer process from the PMU input to its output: when the internal DC/DC converter is off, C_1 charges and V_{IN} (=

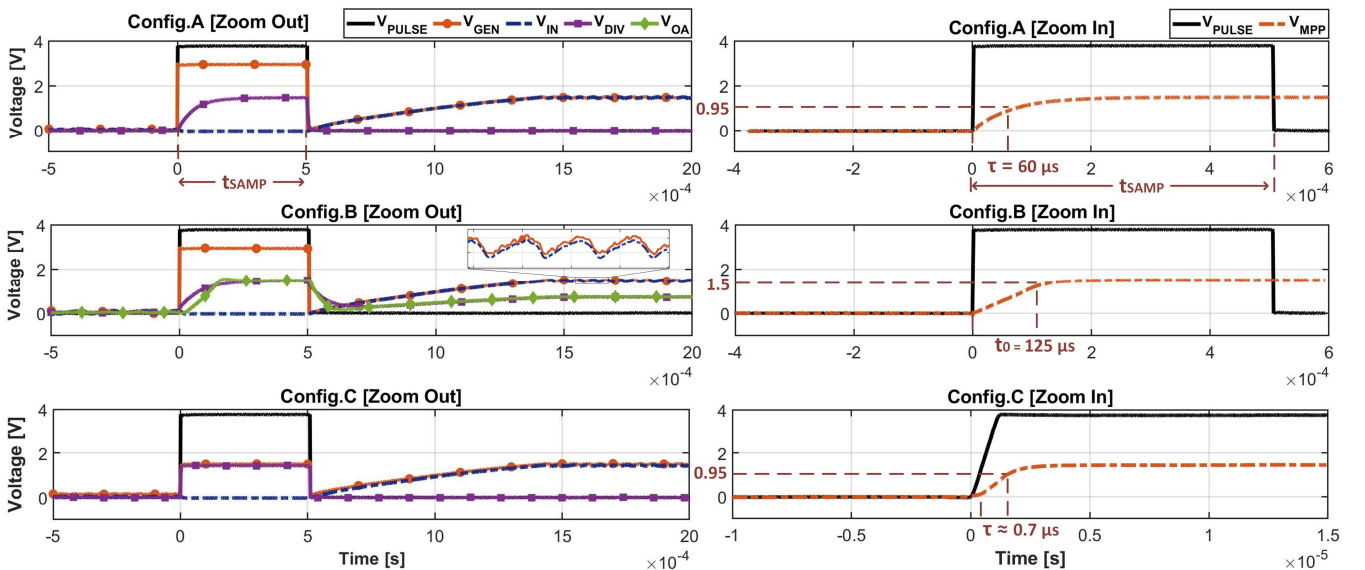


Fig. 5. Dynamic test of the sampling circuitry of the three proposed configurations. Left: zoomed-out view showing V_{PULSE} (solid line), V_{GEN} (circle marker), V_{IN} (dashed line), V_{DIV} (square marker), and V_{OA} (diamond marker). Right: zoomed-in view of V_{MPP} (dashed line) and V_{PULSE} (solid line).

V_{GEN}) increases; contrariwise, when the converter is on and transfers energy to the output, C_1 discharges and V_{IN} decreases. V_{DIV} decreases to 0 V in config. A and C because V_{GEN} is disconnected. However, in config. B, it follows $V_{\text{GEN}}/2$ after some settling time given by τ and V_{OA} is again initially subjected to the OA SR.

The right plots show a zoom-in of V_{PULSE} and V_{MPP} . In all the configurations and during t_{SAMP} , V_{MPP} reaches 1.5 V from an initial value of 0 V, as previewed. In config. A, $\tau = 60 \mu\text{s}$ is marked, hence t_{SAMP} is $\geq 8\tau$, ensuring that V_{MPP} reaches 1.5 V with a negligible error. In config. B, V_{MPP} linearly increases to 1.5 V in about 125 μs (t_0), hence within t_{SAMP} , due to the OA SR. The small peak in V_{OA} (left plot) is mitigated thanks to R_{ISO} . In config. C, a fast $\tau \approx 0.7 \mu\text{s}$ is identified (notice that a different temporal scale is used). Hence, a much lower value of t_{SAMP} could be used to reduce the losses due to the opening of the EH source. After t_{SAMP} , V_{MPP} stabilizes at 1.5 V.

V. PERFORMANCE OF THE POWER MANAGEMENT UNITS

This section shows the PMU experimental performance of the four PMU configurations. First, the three proposed configs. were compared at a fixed r_s and r_M (section V.A). Second, config. C, the configuration with more room for fast-sampling, was optimized following the design criteria of section III.B and then tested at different sampling rates (section V.B). These results were compared with those obtained in section II.A using the analytical expressions. Finally, config. C was tested with a WEC placed on a linear shaker emulating sea conditions (section V.C). Config. R was also used in sections V.A and V.C to assess the achieved improvement of the proposed configurations. In sections V.A and V.B, the FG with the added external resistor was used ($R_G \sim 127 \Omega$) and set to provide a sinusoid with offset, according to (1), with $V_{\text{DC}} = 2 \text{ V}$ and $V_{\text{AC}} = 1 \text{ V}$ and a frequency between 1.8 Hz and 2 Hz to emulate a small-scale WEC under sea-wave excitation [4]. So, from (2), $P_{\text{MPP}} = 8.86 \text{ mW}$. Instead, in section V.C, the WEC presented

in [4] was used under an emulated sea environment. In all sections V_{PULSE} was provided by the DAQ and the four-channel oscilloscope was used to measure V_{GEN} , V_{BAT} , I_{IN} and I_{OUT} . The currents were estimated with a couple of shunt resistors (0.5Ω , 3.3Ω), placed at the test points defined in Fig. 4 (I_{IN} , I_{OUT}), and associated current sense amplifiers (CSAs). The respective oscilloscope channels were placed at the outputs of the CSAs. Then, input and output powers were respectively calculated as $P_{\text{IN}} = V_{\text{GEN}} \cdot I_{\text{IN}}$ and $P_{\text{OUT}} = V_{\text{BAT}} \cdot I_{\text{OUT}}$. To properly estimate the average powers and currents, 5 seconds of data were measured for configurations A, B, and C and 200 seconds for config. R. The set-up of the shunt resistors and CSAs is fully described in Section III of ref. [17].

A. Comparison between configurations

Configurations A, B, and C were assessed with a $T_{\text{MPPT}} = 24 \text{ ms}$, $t_{\text{SAMP}} = 0.5 \text{ ms}$, and $f_{\text{EH}} = 1.8 \text{ Hz}$. So, $r_s = 1/48$ and $r_M = 0.0434$ (about 23 samples per period of the signal source). Fig. 6 shows two seconds of measured data from config. A. As can be seen, when the PMU disconnects the FG output every 24 ms, V_{GEN} rises to V_{OC} (1-3 V) during t_{SAMP} and then settles to $V_{\text{OC}}/2$ (0.5-1.5 V) during t_{HARV} , following the behavior shown in Fig. 1. This behavior is different for config. C, where V_{GEN} does not rise to V_{OC} but follows $V_{\text{OC}}/2$ because the presence of R_Z . During t_{SAMP} , both I_{IN} and I_{OUT} drop to zero. During t_{HARV} , I_{IN} is around $V_{\text{OC}}/(2R_G)$, thus between 3.9 and 11.8 mA. Experimental values of I_{OUT} mainly agree with those estimated from $\eta I_{\text{IN}} V_{\text{IN}} / V_{\text{BAT}}$, being η the efficiency of the ADP5092 IC ($\sim 80\%$

TABLE III. PERFORMANCE OF THE FOUR PMU CONFIGURATIONS.

Config.	T_{MPPT} (ms)	V_{GEN} (V)	P_{IN} (mW)	P_{OUT} (mW)	η (%)
A	24.1	1.012	8.42	7.42	88.2
B	24.1	1.012	8.41	7.38	87.7
C	24.1	0.959	8.58	7.34	85.6
R	16k	0.984	7.21	6.13	85.0

V_{GEN} , P_{IN} and P_{OUT} : Mean values.

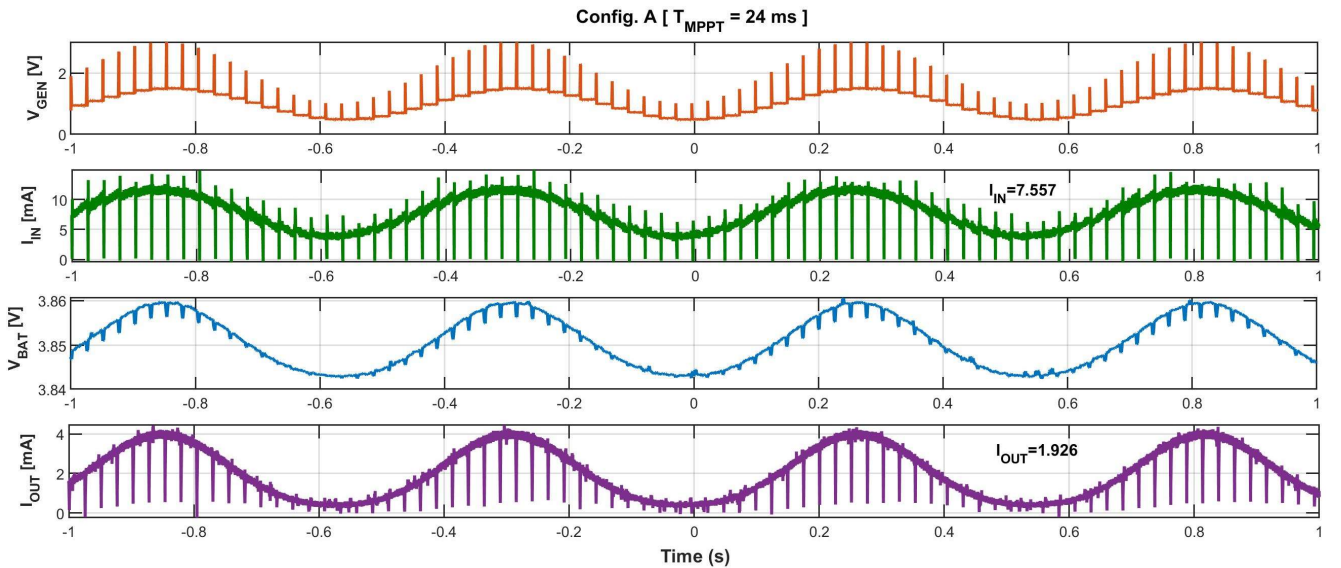


Fig. 6. Acquired waveforms (2 s) for config. A with $T_{\text{MPPT}} = 24 \text{ ms}$. From top to bottom: V_{GEN} , I_{IN} , V_{BAT} , and I_{OUT} . For this test, V_{OC} was set between 1-3 V and T_{EH} at 1.8 Hz.

90 % from the datasheet). V_{BAT} shows a small sinusoidal ripple (< 20 mV) due to the variation of I_{OUT} and the shunt resistor (3.3Ω) used to measure it.

TABLE III presents a summary of the experimental results, showing the averaged values of V_{GEN} , P_{IN} and P_{OUT} . The efficiency (η) has been obtained as $P_{\text{OUT}}/P_{\text{IN}}$ and includes the efficiency of the ADP5092 IC as well as the power wasted by the sampling circuitry (for config. A, B, and C) and by the input stage resistors but not the capability in harvesting the maximum power from the signal source. Configs. A and B present very similar results. Both have negligible losses due to the resistor divider with the efficiency being slightly smaller in config. B (just 0.5 %), in part because some additional power is wasted in the OA. Config. C presents higher P_{IN} (near the calculated P_{MPP}) but lower P_{OUT} than configs. A and B. The increase in P_{IN} is justified by the power wasted in R_Z during t_{SAMP} (0.186 mW nominally), which does not contribute to P_{OUT} . The lower value of P_{OUT} could be caused by the lower average value achieved in V_{GEN} (0.959 V), maybe due to a mismatch between R_G and R_Z , which would lead to a suboptimal working voltage for V_{IN} (lower than $V_{\text{OC}}/2$). Anyhow, P_{OUT} is just 1 % lower than that achieved in config. A. Finally, config. R presents the worst results, as expected. P_{IN} and P_{OUT} are 17 % and 21 % higher in config. A than in the config. R. This happens since T_{MPPT} is much higher than T_{EH} , leading to a significant reduction of the harvested energy.

B. Effect of the sampling time and period

Config. C was chosen to perform further tests since it has similar output power to configs. A and B and presents more

room for the reduction of t_{SAMP} , thus allowing the fastest f_{MPPT} . For the tests, C_{SAMP} was reduced to 1 nF to achieve $\tau = 70$ ns, f_{EH} was set to 2 Hz ($T_{\text{EH}} = 500$ ms), and r_M was varied from 1/4 to 1/80, so f_{MPPT} was varied from 8 Hz to 160 Hz (i.e., T_{MPPT} from 125 ms to 6.25 ms).

A first test was performed with $r_S = 0.1$ %, so t_{SAMP} was correspondingly varied from 125 μs to 6.25 μs . Fig. 7 shows a 2 s interval of V_{GEN} for four cases of $1/r_M$. As $1/r_M$ increases (T_{MPPT} decreases and f_{MPPT} increases), V_{GEN} better follows the sinusoidal shape of $V_{\text{OC}}/2$. Fig. 8 (left) shows the measured P_{IN} (dashed line) normalized to P_{MPP} (8.86 mW) as well the analytical results from (3) (solid line) normalized to P_{MAX} (8.92 mW using (4)), as shown in Fig. 2 from Section II.B. This different normalization compensates for the small error in the piecewise quadratic approximation. As can be seen, there is an excellent match between the analytical and experimental results, which validates the model presented in the Appendix and (3). Power rises to a maximum as r_M decreases (f_{MPPT} increases). Since the drained power through R_Z during t_{SAMP} is negligible (just $r_S = 0.1$ %), P_{IN} , which includes it, was used for the experimental results and $r_S = 0$ was considered for the analytical results in (3).

A second test was performed using $r_S r_M = \frac{t_{\text{SAMP}}}{T_{\text{EH}}} = 10^{-3}$, so $t_{\text{SAMP}} = 500$ μs . So, decreasing r_M increases r_S and thus the percentage of time sampling without harvesting energy from the EH source. As before, Fig. 8 (right) shows the normalized measured (dashed line) and analytical results (solid line). Since in this case the wasted power across R_Z during sampling is not negligible (r_S up to 8 % for $r_M = 1/80$), P_{OUT}/η has been used

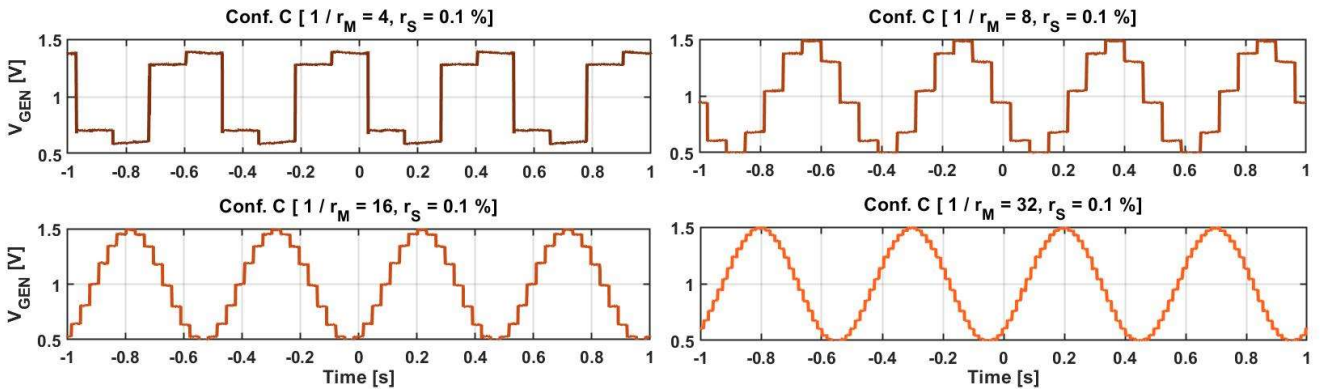


Fig. 7. Acquired V_{GEN} during 2 s in config. C for $1/r_M = 4, 8, 16$ and 32 . All four cases belong to scenario one, where $T_{\text{EH}} = 2$ Hz, $V_{\text{OC}} = 1\text{-}3$ V and $r_S = 0.1\%$.

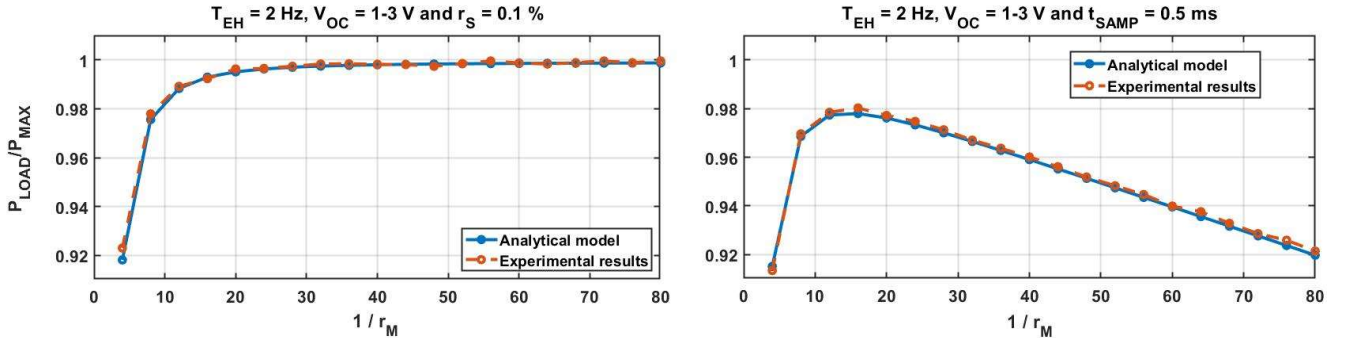


Fig. 8. Normalized harvested power versus $1/r_M$ with config. C for two sampling scenarios according to analytical approximation in (3) (solid line) and experimental results (dashed line). At left, $r_S = 0.1$ %, and at right, $r_S r_M = 10^{-3}$.

instead P_{IN} for the experimental results; otherwise the losses during the sampling time would not be discounted. The mean η obtained in the first test (= 87.9 %) was used. The analytical results also discount the losses ($r_S \neq 0$). Again, theoretical and experimental results greatly match. As before, increasing $1/r_M$ (f_{MPPT} increasing) increases the normalized power but in this case r_S also increases, which increases the time percentage sampling and thus the losses. Thus, a trade-off exists and an optimum value of r_M exists which leads to a maximum value of the normalized power. For $r_M < 1/20$, the normalized power loss is r_S .

C. WEC test

Fig. 9 (right) shows the WEC presented in [17] with the description of the different parts. It consists of a double pendulum containing an arm with a proof mass guaranteeing the alignment of the main body with the wave's direction. The arm is articulated to a ring (main body) which is in turn articulated to the drifter, so it participates in the ring oscillation relative to the drifter. A gear train is coupled to the ring. Through that train, energy is accumulated in a flywheel which drives a DC electrical generator.

The left side of Fig. 9 shows the experimental set-up of this section. A linear shaker (APS 129) with controllable motion was used to emulate the drifter's movement under a sea environment. The WEC was attached to the shaker's moving platform with the device's pendulum aligned to the movement axis. A function generator provided a sinusoidal wave used to control the shaker's acceleration amplitude and frequency, set at 2 Hz. The Arduino-based EH monitoring system presented in [17], which includes an inertial measurement unit (IMU), was used to measure the acceleration of the platform and tune the function generator to achieve an acceleration with peak-to-peak amplitude of 0.4 g, similar to that reported in [4] from a drifter under sea-wave excitation. The WEC's output was connected

to the PMU. Two PMU configurations were used for this test: config. R and config. C with $f_{MPPT} = 60$ Hz ($r_M = 1/30$) and $r_S = 0.1$ %.

Fig. 10 presents the experimental results of V_{GEN} and P_{OUT} using configs. C (left) and R (right), with a zoom-in window of 4 and 16 seconds (one sampling period for config R), respectively. The averaged P_{OUT} is also plotted. The WEC's V_{OC} signal under this test excitation was also measured (not shown) and had a sinusoidal-shape with V_{DC} around 2 V and V_{AC} around 1 V.

Fig. 10 (left) shows how config. C closely follows the MPP every 1/60 ms. V_{GEN} has sinusoidal-shape in concordance with the shaker's acceleration, as happened in [5], with a value between 0.5 and 1.5 V ($V_{OC} = 1-3$ V). In this case, V_{GEN} does not rise to V_{OC} for each sample due to the presence of R_Z . P_{OUT} presents a square sinusoidal-shape following the pendulum's back-and-forward motion. Thanks to the flywheel that keeps the generator rotating, P_{OUT} has a positive offset.

Fig. 10 (right) shows how config. R only samples V_{OC} once every 16 seconds so just one sampling event can be seen. Before and after the sampling event, V_{MPP} is fixed to 1.3 V and 0.8 V, respectively, but could be anywhere between 0.5 and 1.5 V. Anyhow, V_{MPP} is not achieved since T_{MPPT} and thus r_M is too large ($r_M = 32$).

TABLE IV presents the averaged V_{GEN} , P_{IN} and P_{OUT} values, as well as the PMU global efficiency. P_{OUT} is 7.68 mW and 6.11 mW for Config. C and R, respectively. Config. C improves P_{OUT} by 25 %, harvesting an additional 1.57 mW under the

TABLE IV. COMPARISON RESULTS OF THE EMULATED WAVE EXCITATION TEST USING THE LINEAR SHAKER.

Config.	T_{MPPT} (ms)	V_{GEN} (V)	P_{IN} (mW)	P_{OUT} (mW)	Eff. (%)
C	1/60	1.00	8.66	7.68	88.7
R	16k	1.08	6.93	6.11	88.2

V_{GEN} , P_{IN} and P_{OUT} : Mean values.

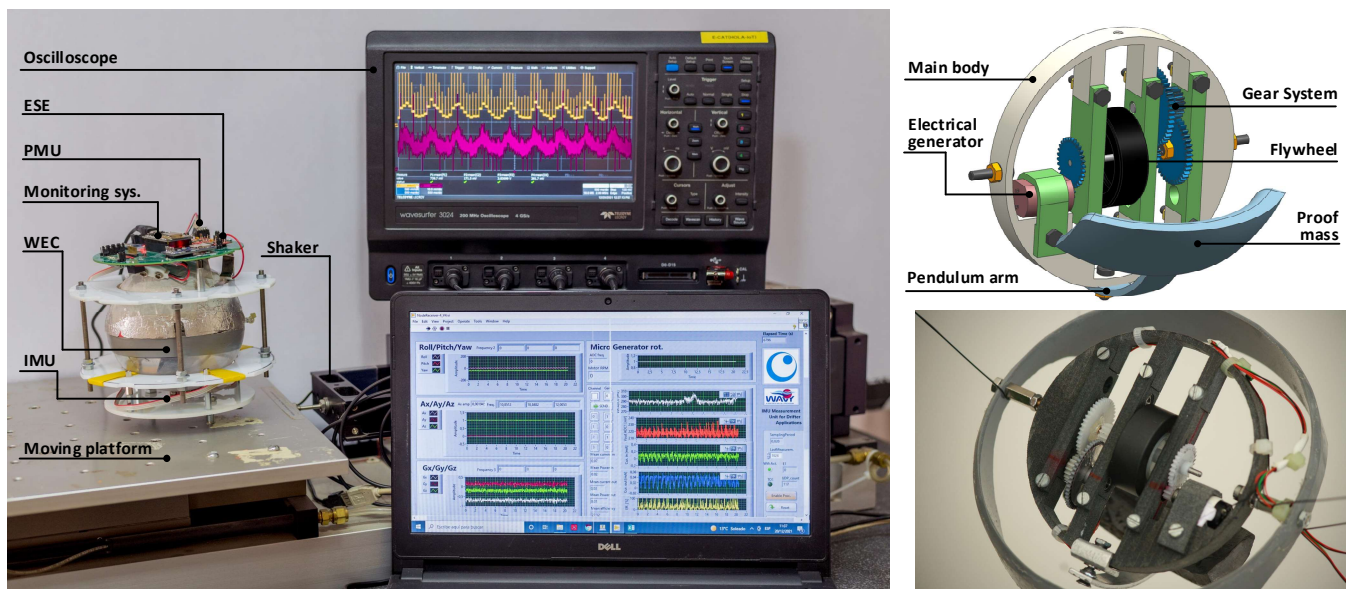


Fig. 9. Experimental set-up for the WEC test. Left: Linear shaker (APS 129) with the WEC attached to the moving platform. Also shown are the PMU, the Arduino-based system and monitoring (PC), and the measuring oscilloscope. Top-right: Architecture of the WEC proposed in [4] with the description of the different parts. Bottom-right: Prototype of the double pendulum WEC device.

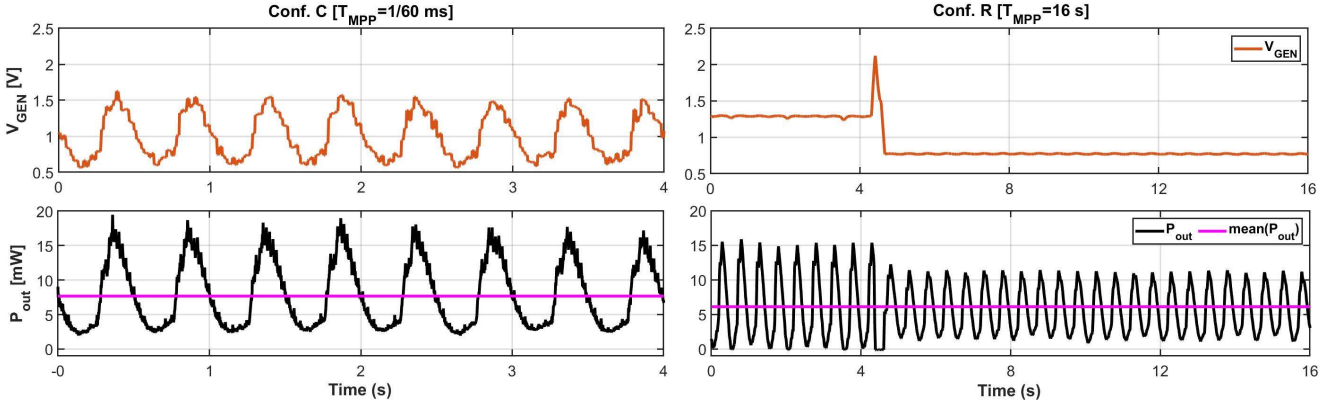


Fig. 10. Experimental results for the WEC test. Left: Config. C with $T_{MPP} = 1/60$ ms. Right: config R. with $T_{MPP} = 16$ s. V_{GEN} (top), P_{OUT} (bottom solid lines), and the average of P_{OUT} (bottom dashed lines) are represented.

same excitation conditions. This percentage matches with [5], where the WEC was placed at the shaker with similar excitation and the fast tracking was emulated by providing an external sinusoidal V_{MPP} to the PMU's CBP pin that approached half the measured V_{OC} . There, the benefit of fast sampling was shown but without the analytical study, proposed circuits, and experimental results that this work provides.

VI. CONCLUSION

The advantages and limitations of increasing the sampling rate in FOCV-MPPT circuits for low-power fast-varying EH sources have been assessed. First, the analytical expressions to optimize the sampling parameters have been provided. Second, the limitations of implementing a fast-sampling FOCV-MPPT circuit have been analyzed and some solutions proposed, resulting in three new configurations, one of them being a novel pseudo-FOCV method. In addition, this circuit achieves the fastest sampling rate by large among the reported works.

A first test has been performed using a 1.8 Hz, 1V to 3 V sinusoidal signal with an output resistance of 127 Ω . The three proposed configurations achieved a similar performance and improved by more than 20 % the harvested energy with respect to a commercial FOCV-PMU with a low sampling rate. A second test has been performed with the novel pseudo-FOCV circuit showing that 1) the harvested power increases with the sampling rate for negligible sampling time (sampling 15 times faster than the source frequency extracts around 99 % of the maximum) and 2) for a fixed sampling time there is an optimum sampling rate where the harvested power is maximum. The first result is also valid for methods other than the FOCV. The experimental and analytical results show very good agreement. Finally, a small-scale WEC prototype has been placed on a linear shaker to emulate the drifter's movement under a sea environment. Results have shown that the proposed configuration improves by 25% the harvested energy from the WEC with respect to the commercial PMU.

APPENDIX

This appendix outlines the derivation of (3), which is an analytical approximation for the power extracted from a sinusoidally varying EH source by a PMU employing FOCV

MPPT. The source is taken to have a constant series output resistance R_G and an open-circuit voltage defined as (1). The following assumptions are made to simplify the analysis:

- Each quarter period of oscillation contains exactly N MPPT updates, i.e. $T_{EH} = 4NT_{MPP}$ where N is a positive integer;
- The first MPPT update in each quarter cycle occurs at the start of the quarter cycle i.e. at the zero-crossing or peak.

It is convenient also to replace the sinusoidal part of V_{OC} by a piecewise quadratic approximation as this allows a closed-form solution to be obtained more easily. The following form will be used to cover the time interval $0 \leq t < T_{EH}$:

$$V_{oc}(t) = \begin{cases} V_{DC} + V_{AC}[1 - (1 - \mu)^2] & \mu = \frac{4t}{T_{EH}}; 0 \leq t < \frac{T_{EH}}{4} \\ V_{DC} + V_{AC}[1 - \mu^2] & \mu = \frac{4t}{T_{EH}} - 1; \frac{T_{EH}}{4} \leq t < \frac{T_{EH}}{2} \\ V_{DC} - V_{AC}[1 - (1 - \mu)^2] & \mu = \frac{4t}{T_{EH}} - 2; \frac{T_{EH}}{2} \leq t < \frac{3T_{EH}}{4} \\ V_{DC} - V_{AC}[1 - \mu^2] & \mu = \frac{4t}{T_{EH}} - 3; \frac{3T_{EH}}{4} \leq t < T_{EH} \end{cases} \quad (A1)$$

The approximation in (A1) is exact at the zero crossings and peaks and has a continuous first derivative. The maximum deviation from the true sinusoidal form is $0.056V_{AC}$.

A. Average extracted power when $t_{SAMP} \rightarrow 0$

For any given V_{OC} waveform, the average power delivered to the PMU by an energy harvester with a constant series output resistance R_G is given by:

$$P = \frac{\overline{[V_{OC}(t) - V_{GEN}(t)]V_{GEN}(t)}}{R_G} \quad (A2)$$

where overbar denotes a time average over the interval of interest. If V_{GEN} is derived by the FOCV-MPPT method, with samples being taken at times $t_n = nT_{MPP}$; $n \in Z$, then we can recast (A2) as:

$$\langle P_n \rangle = \frac{1}{T_{MPP}} \int_{t_n + t_{SAMP}}^{t_n + T_{MPP}} \left[V_{OC}(t) - \frac{V_{OC}(t_n)}{2} \right] \frac{V_{OC}(t_n)}{2R_G} dt \quad (A3)$$

where P_n is the average output power over the n^{th} sampling interval, $t_n \leq t < t_{n+1}$, and $\langle P_n \rangle$ is the arithmetic mean of the P_n values over the time interval of interest. Note that in (A3) it

is assumed that any deviation of V_{GEN} from the value at the start of the sampling interval is negligible; this is a good assumption as t_{SAMP} is small compared to the EH oscillation period T_{EH} .

Then, we continue by considering the average power extracted over the first quadrant or quarter-cycle in the limit where the MPPT sampling time is negligible. According to the simplifying assumptions, MPPT sampling will occur at the discrete times $t_n = nT_{\text{MPPT}}$ where $n = \{0, 1, 2, \dots, (N-1)\}$, and the corresponding values of μ from (A1) will be $\mu_n = \frac{4nT_{\text{MPPT}}}{T_{\text{EH}}} = \frac{n}{N}$. We can therefore express the source voltage in the n^{th} MPPT interval (i.e. the time interval $t_n \leq t < t_{n+1}$) as:

$$V_{\text{OC}}(nT_{\text{MPPT}} + \sigma T_{\text{MPPT}}) = V_{\text{DC}} + V_{\text{AC}} \left[1 - \left(1 - \frac{n}{N} - \frac{\sigma}{N} \right)^2 \right]; \quad (A4)$$

$$0 \leq \sigma < 1$$

Now, at the start of the n^{th} MPPT interval, the EH output voltage (also the PMU input voltage) is set to $\frac{V_{\text{OC}}(nT_{\text{MPPT}})}{2}$ and it remains at this level until the next update. The instantaneous extracted power during the n^{th} MPPT interval is therefore:

$$P_{1n} = \frac{V_{\text{DC}} + V_{\text{AC}} \left[1 - \left(1 - \frac{n}{N} \right)^2 \right]}{2R_G} \left\{ V_{\text{DC}} + V_{\text{AC}} \left[1 - \left(1 - \frac{n}{N} - \frac{\sigma}{N} \right)^2 \right] - \frac{V_{\text{DC}} + V_{\text{AC}} \left[1 - \left(1 - \frac{n}{N} \right)^2 \right]}{2} \right\} \quad (A5)$$

$$= \frac{V_{\text{DC}} + V_{\text{AC}} \left[1 - \left(1 - \frac{n}{N} \right)^2 \right]}{2R_G} \left\{ \frac{V_{\text{DC}}}{2} + \frac{V_{\text{AC}}}{2} \left[1 + \left(1 - \frac{n}{N} \right)^2 \right] - V_{\text{AC}} \left(1 - \frac{n}{N} - \frac{\sigma}{N} \right)^2 \right\}$$

The average extracted power over the n^{th} MPPT interval is then obtained as:

$$\bar{P}_{1n} = \int_0^1 P_{1n} d\sigma = \frac{V_{\text{DC}} + V_{\text{AC}} \left[1 - \left(1 - \frac{n}{N} \right)^2 \right]}{2R_G} \left\{ \frac{V_{\text{DC}}}{2} + \frac{V_{\text{AC}}}{2} \left[1 + \left(1 - \frac{n}{N} \right)^2 \right] + \frac{NV_{\text{AC}}}{3} \left(1 - \frac{n}{N} - \frac{1}{N} \right)^3 - \frac{NV_{\text{AC}}}{3} \left(1 - \frac{n}{N} \right)^3 \right\} \quad (A6)$$

which, after some manipulation, can be recast as:

$$\bar{P}_{1n} = \frac{V_{\text{DC}}^2}{4R_G} + \frac{V_{\text{DC}}V_{\text{AC}}}{R_G} \left\{ \frac{1}{2} - \frac{1}{6N^2} + \frac{\left(1 - \frac{n}{N} \right)}{2N} - \frac{\left(1 - \frac{n}{N} \right)^2}{2} \right\} + \frac{V_{\text{AC}}^2}{R_G} \left\{ \frac{1}{4} - \frac{1}{6N^2} + \frac{\left(1 - \frac{n}{N} \right)}{2N} - \left(\frac{1}{2} - \frac{1}{6N^2} \right) \left(1 - \frac{n}{N} \right)^2 - \frac{\left(1 - \frac{n}{N} \right)^3}{2N} + \frac{\left(1 - \frac{n}{N} \right)^4}{4} \right\} \quad (A7)$$

The average extracted power over the first quadrant can now be obtained by averaging the N values of \bar{P}_{1n} corresponding to $n = \{0, 1, 2, \dots, (N-1)\}$. Here we can make use of the standard results for sums of powers [19]. In particular, if $\langle \rangle$ denotes the arithmetic mean then:

$$\left\langle \left(1 - \frac{n}{N} \right) \right\rangle = 1 - \frac{1}{N^2} \sum_0^{N-1} n = 1 - \frac{N-1}{2N} = \frac{N+1}{2N} \quad (A8)$$

$$\left\langle \left(1 - \frac{n}{N} \right)^2 \right\rangle = \frac{(N+1)(2N+1)}{6N^2} \quad (A9)$$

$$\left\langle \left(1 - \frac{n}{N} \right)^3 \right\rangle = \frac{(N+1)^2}{4N^2} \quad (A10)$$

$$\left\langle \left(1 - \frac{n}{N} \right)^4 \right\rangle = \frac{(N+1)(2N+1)(3N^2+3N-1)}{30N^4} \quad (A11)$$

Replacing each term of the form $\left(1 - \frac{n}{N} \right)^m$ in (A7) by its mean value from (A8), and after some simplification, the average extracted power over the first quadrant is obtained as:

$$\bar{P}_1 = \frac{V_{\text{DC}}^2}{4R_G} + \frac{V_{\text{DC}}V_{\text{AC}}}{3R_G} + \frac{V_{\text{AC}}^2}{R_G} \left\{ \frac{2}{15} - \frac{1}{9N^2} - \frac{1}{24N^3} + \frac{7}{360N^4} \right\} \quad (A12)$$

If the preceding steps are repeated for the other three quadrants, similar results are obtained but with some changes of sign. The results for all four quadrants are encapsulated by the following expression:

$$\bar{P}_q = \frac{V_{\text{DC}}^2}{4R_G} - \frac{(-1)^{\text{rnd}(\frac{q}{2})} V_{\text{DC}}V_{\text{AC}}}{3R_G} + \frac{V_{\text{AC}}^2}{R_G} \left\{ \frac{2}{15} - \frac{1}{9N^2} + \frac{(-1)^q}{24N^3} + \frac{7}{360N^4} \right\} \quad (A13)$$

where q represents the quadrant number and $\text{rnd}(\cdot)$ denotes rounding to the nearest integer.

Finally, the overall average extracted power is obtained as the arithmetic mean of the four quadrant averages. This gives:

$$\bar{P} = \frac{V_{\text{DC}}^2}{4R_G} + \frac{V_{\text{AC}}^2}{R_G} \left\{ \frac{2}{15} - \frac{1}{9N^2} + \frac{7}{360N^4} \right\} \quad (A14)$$

We note that \bar{P} increases monotonically with N which is as expected if the sampling time is negligible. The maximum value of \bar{P} , approached as $N \rightarrow \infty$, corresponds to ideal MPP tracking and is given by

$$\max\{\bar{P}\} = \frac{V_{\text{DC}}^2}{4R_G} + \frac{2}{15} \frac{V_{\text{AC}}^2}{R_G} \quad (A15)$$

This result (equivalent to (4) using α and P_{DC}) is slightly different from the standard result for an offset sinusoidal source given by (2) in the main text because of the piecewise quadratic approximation used here.

B. Effect of finite sampling time

In practice the sampling time t_{SAMP} is finite and in FOCV MPPT no power is delivered to the load during sampling. If we assume that $t_{\text{SAMP}} \ll T_{\text{EH}}$ then we can take the source voltage to be constant during sampling. Also, since sampling coincides with setting the output voltage to V_{MPP} , we can assume that the load presented by the PMU would have been perfectly matched during the sampling interval, had it remained connected. With these assumptions, the energy forfeited during the n^{th} sampling event in the first quadrant will be:

$$U_{1n} = t_{\text{SAMP}} \frac{V_{\text{OC}}^2(nT_M)}{4R_G} = t_{\text{SAMP}} \frac{\left\{ V_{\text{DC}} + V_{\text{AC}} \left[1 - \left(1 - \frac{n}{N} \right)^2 \right] \right\}^2}{4R_G} = \quad (A16)$$

$$t_{\text{SAMP}} \left\{ \frac{V_{\text{DC}}^2}{4R_G} + \frac{V_{\text{DC}}V_{\text{AC}}}{2R_G} \left[1 - \left(1 - \frac{n}{N} \right)^2 \right] + \frac{V_{\text{AC}}^2}{4R_G} \left[1 - 2 \left(1 - \frac{n}{N} \right)^2 + \left(1 - \frac{n}{N} \right)^4 \right] \right\}$$

The resulting loss in average power over the first quadrant is:

$$\bar{L}_1 = \frac{4}{T_{\text{EH}}} N \langle U_{1n} \rangle = r_S \left\langle \frac{U_{1n}}{t_{\text{SAMP}}} \right\rangle \quad (A17)$$

Replacing each term of the form $\left(1 - \frac{n}{N} \right)^m$ in (A16) by its

mean value from (A8), and after some simplification, (A17) can be recast as:

$$\bar{L}_1 = r_s \left\{ \frac{V_{DC}^2}{4R_G} + \frac{V_{DC}V_{AC}}{R_G} \left[\frac{1}{3} - \frac{1}{4N} - \frac{1}{12N^2} \right] + \frac{V_{AC}^2}{R_G} \left[\frac{2}{15} - \frac{1}{8N} - \frac{1}{120N^4} \right] \right\} \quad (A18)$$

Repeating the above analysis for the other three quadrants gives similar results with some sign changes, and the results for all four quadrants are encapsulated by the following expression:

$$\bar{L}_q = r_s \left\{ \frac{V_{DC}^2}{4R_G} - \frac{(-1)^{\text{nd}(\frac{q}{2})} V_{DC}V_{AC}}{R_G} \left[\frac{1}{3} + \frac{1}{4N} - \frac{1}{12N^2} \right] + \frac{V_{AC}^2}{R_G} \left[\frac{2}{15} + \frac{(-1)^q}{8N} - \frac{1}{120N^4} \right] \right\} \quad (A19)$$

The overall loss of average extracted power due to sampling is obtained by evaluating the arithmetic mean of the four quadrant averages. This gives:

$$\bar{L} = r_s \left\{ \frac{V_{DC}^2}{4R_G} + \frac{V_{AC}^2}{R_G} \left[\frac{2}{15} - \frac{1}{120N^4} \right] \right\} \quad (A20)$$

Combining (A14) and (A20), the average power extracted by the PMU when the sampling time is finite is:

$$P_{LOAD} \approx \bar{P} - \bar{L} = \left[\frac{V_{DC}^2}{4R_G} + \frac{2V_{AC}^2}{15R_G} \right] (1 - r_s) - \left[\frac{V_{AC}^2}{9R_G} \right] \frac{1}{N^2} + \left[\frac{V_{AC}^2}{R_G} \left(\frac{7 + 3r_s}{360} \right) \right] \frac{1}{N^4} \quad (A21)$$

Using the substitutions $P_{DC} = \frac{V_{DC}^2}{4R_G}$, $r_M = \frac{1}{4N}$ and $\alpha = \frac{V_{AC}}{V_{DC}}$, the expression given in (3) is obtained. The value of P_{LOAD} given by (A26) is exact for the waveform described by (A6) in the limit as $t_{SAMP} \rightarrow 0$.

REFERENCES

[1] F. Faraz, C. Ghenai, and M. Bettayeb, "Maximum power point tracking and photovoltaic energy harvesting for Internet of Things: A comprehensive review," *Sustain. Energy Technol. Assessments*, vol. 47, no. July, p. 101430, 2021.

[2] D. Dondi, A. Bertacchini, D. Brunelli, L. Larcher, and L. Benini, "Modeling and optimization of a solar energy harvester system for self-powered wireless sensor networks," *IEEE Trans. Ind. Electron.*, vol. 55, no. 7, pp. 2759–2766, 2008.

[3] M. Shi, A. S. Holmes, and E. M. Yeatman, "Nonlinear Wind Energy Harvesting Based on Mechanical Synchronous Switch Harvesting on Inductor," in *21st International Conference on Solid-State Sensors, Actuators and Microsystems (Transducers) - Virtual*, 2021, vol. 1.

[4] M. Carandell, D. M. Toma, P. Alevras, M. Gasulla, J. del Río, and A. Barjau, "Nonlinear Dynamic Analysis of a Small-Scale Pendulum-Type Wave Energy Converter for Low-Power Marine Monitoring Applications," in *14th European Wave and Tidal Energy Conference, EWTEC - Plymouth*, 2021.

[5] M. Carandell, D. M. Toma, J. del Río, and M. Gasulla, "Optimum MPPT Strategy for Low-Power Pendulum-Type Wave Energy Converters," in *IEEE Sensors Conference - Rotterdam*, 2020.

[6] L. Costanzo, A. Lo Schiavo, and M. Vitelli, "Performance of the Open-Circuit Voltage MPPT Technique for Piezoelectric Vibration Harvesters," in *Proceedings - IEEE International Symposium on Circuits and Systems*, 2020, no. 1, pp. 0–4.

[7] F. I. Simjee and P. H. Chou, "Efficient charging of supercapacitors for extended lifetime of wireless sensor nodes," *IEEE Trans. Power Electron.*, vol. 23, no. 3, pp. 1526–1536, 2008.

[8] H. Shao, X. Li, C. Y. Tsui, and W. H. Ki, "A novel single-inductor dual-input dual-output DC-DC converter with PWM control for solar energy harvesting system," *IEEE Trans. Very Large Scale Integr. Syst.*, vol. 22, no. 8, pp. 1693–1704, 2014.

[9] C. G. Yu, "A vibrational energy harvesting interface circuit with maximum power point tracking control," *Int. J. Appl. Eng. Res.*, vol. 12, no. 22, pp. 12102–12107, 2017.

[10] A. Shrivastava, N. E. Roberts, O. U. Khan, D. D. Wentzloff, and B. H. Calhoun, "A 10 mV-Input boost converter with inductor peak current control and zero detection for thermoelectric and solar energy harvesting with 220 mV Cold-Start and -14.5 dBm, 915 MHz RF Kick-Start," *IEEE J. Solid-State Circuits*, vol. 50, no. 8, pp. 1820–1832, 2015.

[11] M. K. Rajendran, V. Priya, S. Kansal, G. Chowdary, and A. Dutta, "A 100-mV-2.5-V burst mode constant on-time-controlled battery charger with 92% peak efficiency and integrated FOCV technique," *IEEE Trans. Very Large Scale Integr. Syst.*, vol. 27, no. 2, pp. 430–443, 2019.

[12] M. Dini, A. Romani, M. Filippi, and M. Tartagni, "A Nanocurrent Power Management IC for Low-Voltage Energy Harvesting Sources," *IEEE Trans. Power Electron.*, vol. 31, no. 6, pp. 4292–4304, 2016.

[13] G. Saini and M. S. Baghini, "An energy harvesting system for time-varying energy transducers with FOCV based dynamic and adaptive MPPT for 30 nW to 4 mW of input power range," *Microelectronics J.*, vol. 114, no. March, p. 105080, 2021.

[14] J. J. Estrada-Lopez, A. Abuellil, A. Costilla-Reyes, M. Abouzied, S. Yoon, and E. Sanchez-Sinencio, "A Fully Integrated Maximum Power Tracking Combiner for Energy Harvesting IoT Applications," *IEEE Trans. Ind. Electron.*, vol. 67, no. 4, pp. 2744–2754, 2020.

[15] M. Balato, L. Costanzo, A. Lo Schiavo, and M. Vitelli, "Optimization of both Perturb & Observe and Open Circuit Voltage MPPT Techniques for Resonant Piezoelectric Vibration Harvesters feeding bridge rectifiers," *Sensors Actuators, A Phys.*, vol. 278, pp. 85–97, 2018.

[16] R. E. Thomas, A. J. Rosa, and G. J. Toussaint, *The analysis and design of linear circuits*, 8th ed. JOHN WILEY & SONS, 2016.

[17] M. Carandell, D. M. Toma, M. Carbonell, J. del Río, and M. Gasulla, "Design and Testing of a Kinetic Energy Harvester Embedded into an Oceanic Drifter," *IEEE Sens. J.*, vol. 20, no. 23, 2020.

[18] S. Fan, R. Wei, L. Zhao, X. Yang, L. Geng, and P. X. L. Feng, "An Ultralow Quiescent Current Power Management System with Maximum Power Point Tracking (MPPT) for Batteryless Wireless Sensor Applications," *IEEE Trans. Power Electron.*, vol. 33, no. 9, pp. 7326–7337, 2018.

[19] A. F. Beardon, "Sums of powers of integers," *Am. Math. Mon.*, vol. 103, no. 3, pp. 201–213, 1996.



Matias Carandell was born in Barcelona, Spain, in 1991. He received a B.Sc. and a M.S. in Industrial Engineering from Universitat Politècnica de Catalunya (UPC), with the specialty of electrical engineering, in 2015. After that, he spent one year at Universidad Técnica Federico Santa María (UTFSM, Chile), working with solar power converters. He is currently doing his Ph.D. in Electronic Engineering at the Remote Acquisition Systems and Data Processing (SARTI) research group, at UPC. His current research interests include energy harvesting in marine environment, energy conditioning systems for autonomous sensors and autonomy concerning Lagrangian Drifter electronics (matias.carandell@upc.edu).



Andrew S. Holmes received the BA degree in natural sciences from Cambridge University in 1987, and the PhD degree in electrical engineering from Imperial College London in 1992. He is currently Professor of Micro-Electro-Mechanical Systems (MEMS) in the Department of Electrical and Electronic Engineering, Imperial College London. His research interests include micro-power generation by energy harvesting, power conditioning for energy harvesters, tribology of micro-scale mechanical systems, novel micro-assembly techniques, and laser processing for MEMS and electronics manufacture (a.holmes@imperial.ac.uk).



Daniel Mihai Toma received a M.Sc. degree in Electrical Engineering from the Technical University “Gheorghe Asachi,” Iasi, Romania, in 2008 and a Ph.D. degree in Electronic Engineering from the Universitat Politècnica de Catalunya (UPC), Barcelona, Spain, in 2012. He is currently a member of the research group Remote Acquisition Systems and Data processing (SARTI), Electronic Engineering Department, UPC. His current research interests include electronic instrumentation, wireless ad hoc networks, interoperability in sensor networks, and synchronization and scheduling (daniel.mihai.toma@upc.edu).



Joaquín del Río was born in Catalonia, Spain, in 1976. He received a B.Sc., M.Sc., and Ph.D. degrees in Telecommunication Engineering and Electronic Engineering from the Universitat Politècnica de Catalunya (UPC), Barcelona, Spain, in 1999, 2002, and 2011, respectively. Since 2001, he has been a Professor in the Electronic

Engineering Department, UPC. He is a member of the research group Remote Acquisition Systems and Data Processing (SARTI). His research focuses on electronic instrumentation, interoperability in marine sensor networks, and wireless sensor networks. Prof. del Río is a member of the National Institute of Standards and Technology (NIST) IEEE1451.2 Working Group and the Smart Ocean Sensors Consortium and PUCK Standard Working Group (SWG). He is involved in numerous projects within the industry and is a National Instruments Certified Instructor for teaching official LabVIEW courses (joaquin.del.rio@upc.edu).



Manel Gasulla was born in Vinaròs, Spain, on May 26th, 1967. He received an Enginyer (M.Eng.) and a Doctor Enginyer (Ph.D.) degrees in Telecommunications from the Universitat Politècnica de Catalunya (UPC BarcelonaTech), Barcelona, in 1992 and 1999, respectively. Since 1993 he has been with UPC, where he is an associate professor, engaged in teaching on Analog and Power Electronics and Electronic Instrumentation. In 2001-2002 he was a Visiting Postdoctoral Fellow at the Electronic Instrumentation Laboratory, Delft University of Technology, The Netherlands. His research interests include capacitive sensors, direct sensor-to-microcontroller interfaces, and energy harvesting and wireless power transfer circuits for autonomous sensors. Presently, he leads the research group e-CAT (Electronic Transducers and Interfaces) at UPC, which focuses on new electronic circuits applied to transducers for signal and power processing with the aim of developing energy-autonomous smart sensors. He is co-author of more than 70 papers in journals and conferences, seven Spanish patents, several chapters in books and the book *Powering Autonomous Sensors* - Springer, 2011 (manel.gasulla@upc.edu).